

Extracting information from ocean color

B. B. Cael¹, Kelsey M Bisson², Emmanuel S Boss³, and Zachary K Erickson⁴

¹National Oceanography Centre

²Oregon State University

³University of Maine

⁴NASA Goddard Space Flight Center

December 8, 2022

Abstract

Products derived from remote sensing reflectances ($R_{rs}(\lambda)$), e.g. chlorophyll, phytoplankton carbon, euphotic depth, or particle size, are widely used in oceanography. Problematically, $R_{rs}(\lambda)$ may have fewer degrees of freedom (DoF) than measured wavebands or derived products. A global sea surface hyperspectral $R_{rs}(\lambda)$ dataset has DoF=4. MODIS-like multispectral equivalent data also have DoF=4, while their SeaWiFS equivalent has DoF=3. Both multispectral-equivalent datasets predict individual hyperspectral wavelengths' $R_{rs}(\lambda)$ within nominal uncertainties. Remotely sensed climatological multispectral $R_{rs}(\lambda)$ have DoF=2, as information is lost by atmospheric correction, shifting to larger spatiotemporal scales, and/or more open-ocean measurements, but suites of $R_{rs}(\lambda)$ -derived products have DoF=1. These results suggest that remote sensing products based on existing satellites' $R_{rs}(\lambda)$ are not independent and should not be treated as such, that existing $R_{rs}(\lambda)$ measurements hold unutilized information, and that future multi- or especially hyper-spectral algorithms must rigorously consider correlations between $R_{rs}(\lambda)$ wavebands.

Extracting information from ocean color

B. B. Cael¹, Kelsey Bisson², Emmanuel Boss³, and Zachary K. Erickson⁴

¹National Oceanography Centre, Southampton, UK

²Oregon State University, Corvallis, OR, USA

³University of Maine, Orono, ME, USA

⁴NOAA Pacific Marine Environmental Laboratory, Seattle, WA, USA

Key Points:

- In situ hyperspectral $R_{rs}(400-700\text{nm})$ have 4 degrees of freedom & are predicted within uncertainties by MODIS & SeaWiFS wavebands.
- Degrees of freedom are lost upscaling to global satellite climatologies and again to $R_{rs}(\lambda)$ -derived products like chlorophyll.
- Information exists in satellite $R_{rs}(\lambda)$ that's underutilized by products' algorithms. Future algorithms must consider correlations carefully.

Corresponding author: B. B. Cael, cael@noc.ac.uk

Abstract

Products derived from remote sensing reflectances ($R_{rs}(\lambda)$), e.g. chlorophyll, phytoplankton carbon, euphotic depth, or particle size, are widely used in oceanography. Problematically, $R_{rs}(\lambda)$ may have fewer degrees of freedom (DoF) than measured wavebands or derived products. A global sea surface hyperspectral $R_{rs}(\lambda)$ dataset has DoF=4. MODIS-like multispectral equivalent data also have DoF=4, while their SeaWiFS equivalent has DoF=3. Both multispectral-equivalent datasets predict individual hyperspectral wavelengths' $R_{rs}(\lambda)$ within nominal uncertainties. Remotely sensed climatological multispectral $R_{rs}(\lambda)$ have DoF=2, as information is lost by atmospheric correction, shifting to larger spatiotemporal scales, and/or more open-ocean measurements, but suites of $R_{rs}(\lambda)$ -derived products have DoF=1. These results suggest that remote sensing products based on existing satellites' $R_{rs}(\lambda)$ are not independent and should not be treated as such, that existing $R_{rs}(\lambda)$ measurements hold unutilized information, and that future multi- or especially hyper-spectral algorithms must rigorously consider correlations between $R_{rs}(\lambda)$ wavebands.

Plain Language Summary

The reflectance of sunlight from the ocean can be observed from satellites and is used to derive many biologically-relevant parameters, such as the concentration of chlorophyll in the upper ocean. Reflectances are currently observed at about ten different wavelengths, but this will soon be expanded to hundreds with the upcoming launch of a new ocean color satellite, PACE, in early 2024. Many new algorithms are being proposed to make use of the wealth of ocean color data which will be provided. However, there are strong correlations between reflectances at different wavelengths; these correlations mean there will be far fewer products that can be independently derived than there will be reflectance wavelengths observed. Here we use a ship-based measurements similar to what will be provided from PACE to suggest that, on a global scale, only a few independent variables can be calculated from hundreds of reflectance wavelengths. Current and past satellites provide a similar amount of independent data to what is projected from PACE. We then show that, on a global scale, a set of six derived parameters only contains one independent piece of information, suggesting that more information exists in ocean color data than is being currently used.

1 Introduction

Ocean color satellites have revolutionized the study of ocean ecology and biogeochemistry in recent decades by providing a near-continuous global picture of surface ocean properties (Hovis et al., 1980; O'Reilly et al., 1998). Satellites measure the spectral radiance emanating from the ocean and atmosphere. Remote sensing reflectance ($R_{rs}(\lambda)$) is obtained following the removal of the contribution of atmospheric and surface effects and normalization to downwelling solar irradiance. Algorithms have been developed to estimate numerous biogeochemically-relevant surface variables from $R_{rs}(\lambda)$, such as chlorophyll concentration (Chl, [$\mu\text{g/L}$]) (O'Reilly et al., 1998; Hu et al., 2012), the spectral slope of the particle size distribution (ξ) (Kostadinov et al., 2009), the concentrations of phytoplankton and particulate organic and inorganic carbon (C_{phyto} , POC, and PIC, [$\mu\text{g/L}$]) (Graff et al., 2015; Evers-King et al., 2017; Mitchell et al., 2017), euphotic layer depth (Z_{eu} [m]) (Lee et al., 2007), and, using additional input variables, net primary production (NPP, [$\text{mg/m}^2\text{d}$]) (Behrenfeld & Falkowski, 1997; Silsbe et al., 2016; Westberry et al., 2008). Such products are used in a wide variety of applications, such as validation of complex ocean ecosystem and biogeochemistry models (Dutkiewicz et al., 2020; Cael et al., 2021) or as inputs for simpler models that predict other variables such as vertical particulate organic carbon fluxes from ocean color (Siegel et al., 2014; Cael et al., 2017; DeVries & Weber, 2017; Nowicki et al., 2022; Bisson et al., 2020).

Existing $R_{rs}(\lambda)$ data are multispectral, meaning they are measured within several individually determined wavebands. Derived products generally rely only on a subset of these wavebands and are commonly expressed as functions of band ratios between just two wavelengths (e.g. Hu et al., 2012). Some algorithms attempt to simultaneously estimate multiple products to match the full spectrum of $R_{rs}(\lambda)$; for example, the Generalized Inherent Optical Properties (GIOP) approach (Werdell et al., 2013) uses known and assumed spectral shapes of backscattering and absorption from different optical constituents to estimate the suite of products that best represents the observed $R_{rs}(\lambda)$. However, the most widely used products, such as for Chl and POC, treat all outputs as independent quantities and are fully empirical.

Correlations between $R_{rs}(\lambda)$ at different wavebands can be quite strong (Huot & Antoine, 2016), depending also on the spatiotemporal scales considered (see §3). This presents multiple potential issues for both users and developers of ocean color derived products. If multiple products are used simultaneously and treated as independent when they are in fact not, this can lead to overconfidence in model skill or miscalculation of uncertainties. An unintended consequence of treating satellite products independently within models is a functional limit on model complexity. Adding different (yet correlated) satellite products to a model can result in model output redundancy (Bisson et al., 2020). These issues will only be exacerbated by the hyperspectral resolution of the next generation of ocean color satellites, namely the Plankton, Clouds, Aerosols and Ecosystems (PACE) satellite scheduled to launch January 2024 (Werdell et al., 2019). In addition to the common suite of multispectral products, PACE also plans to move beyond chlorophyll and enable characterizations of phytoplankton communities (e.g. Chase et al., 2017), substantially increasing the number of products available from $R_{rs}(\lambda)$.

The strong correlations among $R_{rs}(\lambda)$ wavelengths can be framed in terms of the degrees of freedom (DoF) of $R_{rs}(\lambda)$ measurements and suites of derived products. DoF represents the effective number of dimensions of a dataset after accounting for correlations and uncertainties between variables and is in essence the number of independent variables in that dataset. It has been shown that the DoF of globally distributed near-surface measured hyperspectral absorption spectra is about five (Cael et al., 2020). This could be considered a possible upper limit for the DoF of satellite-measured $R_{rs}(\lambda)$ given higher uncertainties on satellite measurements – particularly associated with atmospheric correction (Bisson et al., 2021; Cael et al., 2020). The DoF of PACE’s hyperspectral measurements might then be expected to be much lower than the number of wavelengths for which it will measure $R_{rs}(\lambda)$, which will appreciably affect how hyperspectral satellite $R_{rs}(\lambda)$ products should be constructed. For both existing and future satellite $R_{rs}(\lambda)$, in other words, understanding the DoF of $R_{rs}(\lambda)$ measurements and derived products is crucial for appropriate usage and optimal construction of such products.

Here we investigate the DoF of $R_{rs}(\lambda)$. We first find that a global sea surface hyperspectral $R_{rs}(\lambda)$ database has four DoF. Coarsening hyperspectral $R_{rs}(\lambda)$ to their MODIS (Moderate Resolution Imaging Spectrometer) equivalent retains four DoF, though the SeaWiFS (Sea-viewing Wide Field of view Sensor) equivalent only has three DoF. Both of these multispectral equivalents can, however, predict individual hyperspectral $R_{rs}(\lambda)$ wavelengths within nominal uncertainties for satellite sensors. We then consider climatological $R_{rs}(\lambda)$ and derived products. We find that both MODIS-Aqua and SeaWiFS $R_{rs}(\lambda)$ have two DoF at the climatological scale, suggesting that $R_{rs}(\lambda)$ complexity is lost either through atmospheric correction, relatively more inclusion of open-ocean data, or averaging over larger scales in space and time. Suites of derived products, however, only retain one DoF. This latter result suggests that derived products should not be treated as independent by users. We close by discussing the substantial implications these findings have for the construction and use of ocean color products, from both existing and future $R_{rs}(\lambda)$.

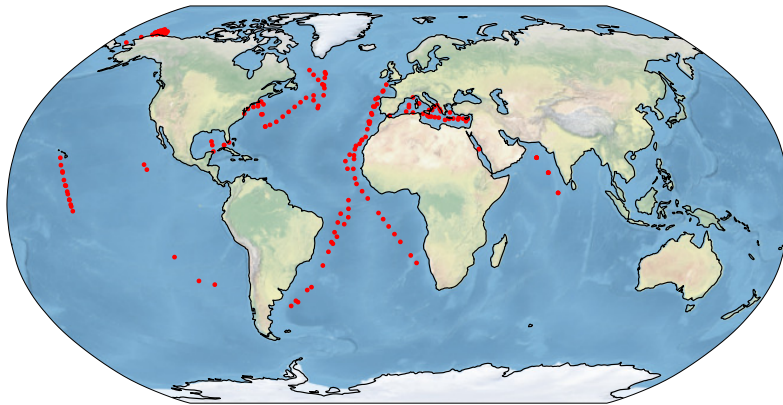


Figure 1. Locations of the 191 stations considered in this study (red dots).

116

2 Sea surface R_{rs} : hyperspectral versus multispectral

117

118

119

120

121

122

123

124

125

126

127

128

129

130

131

132

We first analyze a global sea surface hyperspectral $R_{rs}(\lambda)$ dataset to determine its DoF and how the DoF depends on spectral resolution (Chase et al., 2017; Kramer et al., 2022). The dataset includes $R_{rs}(\lambda)$ data at 191 locations at an effective 3.35 nm resolution (Chase et al., 2017) from 400–800 nm, linearly interpolated to 1 nm (Figure 1). We trimmed spectra to 700nm due to the large fraction of missing values $>700\text{nm}$; note that most of the non-empty values $>700\text{nm}$ are zeros and the non-zero-non-empty values, with a median of $<4 \times 10^{-5} \text{ sr}^{-1}$, have very small signal-to-noise ratios. The dataset includes measurements taken from 2004 to 2018 evenly distributed across months of the year, and from all major ocean basins ranging in latitude from 41°S to 74°N . We also compare these data to their MODIS-Aqua and SeaWiFS multispectral equivalents by convoluting the hyperspectral $R_{rs}(\lambda)$ with the MODIS-Aqua and SeaWiFS spectral response functions (available at https://oceancolor.gsfc.nasa.gov/docs/rsr/HMODISA_RSRs.txt and https://oceancolor.gsfc.nasa.gov/docs/rsr/SeaWiFS_RSRs.txt) to generate 10-waveband and 6-waveband datasets which correspond to what each instrument would have measured from the same optical input that the radiometer received when generating the hyperspectral $R_{rs}(\lambda)$ data.

133

134

135

136

137

138

139

140

141

142

143

144

145

146

147

148

149

150

151

We then apply principal component analysis (PCA) (Wold et al., 1987) to these 301-, 10- and 6-dimensional $R_{rs}(\lambda)$ datasets. PCA is a widely used method to reduce the dimensionality of datasets by identifying orthogonal vectors that explain the most variance in the data. PCA is linear in nature, which may result in an overestimation of effective dimensions by poorly approximating non-linear relationships between variables (e.g. a PCA performed on the pair (x, y) where $y = x^2$ will yield two DoF). Nonlinear generalizations do exist (Weinberger et al., 2004; Scholz et al., 2008), though these are less widely applied due to their additional complexity and computational requirements that make interpretation challenging. One may therefore consider the DoF we report to be upper bounds. We perform a PCA on each $R_{rs}(\lambda)$ dataset, standardizing each first by subtracting from each waveband its mean and then dividing by its standard deviation. This results in a percentage of total variance explained by each component. We use the broken-stick rule to choose the DoF, which states that the DoF is equal to the number of components that explain more variance than would be expected by randomly distributed data; this method was shown to be more consistent than a suite of others in a comparison (Jackson, 1993). These results can be shown visually as a ‘scree’ plot, which plots the percentage of variance explained by each component and for randomly distributed data; the DoF is the number of components with a higher percentage of variance explained than would be expected for randomly distributed data. Our figures also visibly demon-

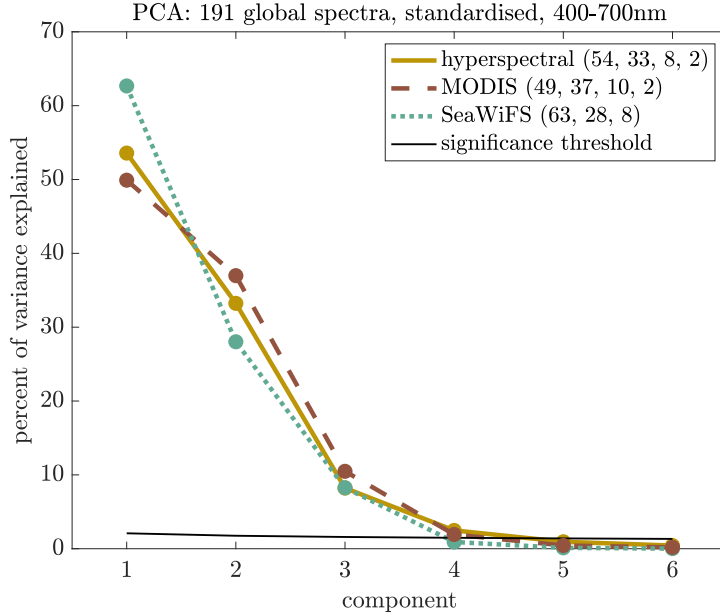


Figure 2. Scree plot of percent variance explained versus component for hyperspectral $R_{rs}(\lambda)$ dataset and MODIS-Aqua and SeaWiFS equivalents calculated from their spectral response functions. Black line indicates broken-stick significance threshold for hyperspectral data; numbers in legend give percent variance explained for each mode above this threshold in each case.

152 strate that one would get the same results from using the scree plot rule, which states
 153 that the DoF is equal to the number of components not sitting on the straight line made
 154 by the higher-order components, and was found to consistently capture the correct DoF
 155 plus one when the first point on this straight line was included (Jackson, 1993).

156 PCA analysis reveals that the hyperspectral in situ $R_{rs}(\lambda)$ dataset has four DoF
 157 (Figure 2); the first four components explain 54%, 33%, 8%, and 2%, totalling 97%, of
 158 the variance. The first four MODIS-Aqua equivalent $R_{rs}(\lambda)$ principal components have
 159 very similar percentages of variance explained: 49%, 37%, 10%, and 2%, totalling 99%
 160 of the total variance. In contrast, the first three SeaWiFS equivalent $R_{rs}(\lambda)$ principal
 161 components explain 63%, 28%, and 8%, totalling 99%, of the variance. This suggests
 162 that the hyperspectral $R_{rs}(\lambda)$ have four DoF, or four independent variables within the
 163 data, and that these four variables are effectively captured when reducing spectral res-
 164 olution to the ten MODIS-Aqua wavebands, but not to the six SeaWiFS wavebands.

165 The ability of coarsened, MODIS-equivalent data to obtain the same number of DoF
 166 as the hyperspectral dataset is further supported by predictions of hyperspectral $R_{rs}(\lambda)$
 167 from multispectral equivalents. To illustrate this, for each hyperspectral wavelength we
 168 perform a multivariate linear regression of $R_{rs}(\lambda)$ at that wavelength regressed against
 169 $R_{rs}(\lambda)$ at each waveband of both the MODIS-Aqua and SeaWiFS equivalent $R_{rs}(\lambda)$. We
 170 then calculate the root-mean-square-error (RMSE) of these regressions. For all wavelengths
 171 below 578 nm in the SeaWiFS case and 582 nm in the MODIS-Aqua case, the RMSE
 172 is smaller – and for many, much smaller – than 5% of the mean $R_{rs}(\lambda)$ at that wavelength,
 173 where 5% is a nominal relative uncertainty for satellite $R_{rs}(\lambda)$ (Figure 3). Even for wave-
 174 lengths greater than this, the RMSE is still very small in absolute terms, $<0.00007 \text{ sr}^{-1}$,
 175 far smaller than the nominal 0.0003 sr^{-1} absolute error for 1km-by-1km pixels for PACE
 176 (Gordon & Wang, 1994). These small errors in predicting hyperspectral $R_{rs}(\lambda)$ from its
 177 multispectral equivalent underscore the extent to which different wavelengths’ $R_{rs}(\lambda)$

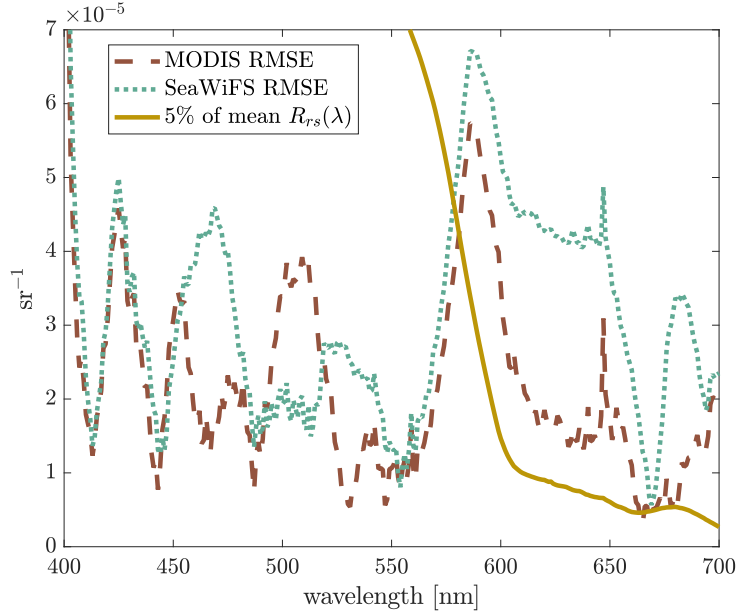


Figure 3. Root-mean-square-error of multivariate linear regressions of each hyperspectral wavelength versus the MODIS-Aqua and SeaWiFS equivalent $R_{rs}(\lambda)$. Solid line is 5% of the mean of each wavelength’s hyperspectral $R_{rs}(\lambda)$.

178 are correlated and demonstrate the ability of MODIS-Aqua equivalent multispectral $R_{rs}(\lambda)$
 179 to preserve the dimensionality of hyperspectral $R_{rs}(\lambda)$. The fact that SeaWiFS-like $R_{rs}(\lambda)$
 180 can accurately predict hyperspectral $R_{rs}(\lambda)$ to within PACE uncertainties but has fewer
 181 DoF than the in situ hyperspectral dataset is a reflection of the lower uncertainty on the
 182 in situ dataset than the expected PACE $R_{rs}(\lambda)$, and suggests that PACE $R_{rs}(\lambda)$ may
 183 have fewer DoF than the in situ hyperspectral dataset.

184 We also note that excluding wavelengths 651–700nm affects the DoF numbers presented here but not our conclusions. A choice of an upper limit of 650nm would be based
 185 on the fact that for all wavelengths above 648nm, >95% of measurements are below 0.0003
 186 sr^{-1} , the nominal uncertainty of a 1km-by-1km pixel for PACE (Gordon & Wang, 1994).
 187 Repeating this analysis over 400–650nm results in hyperspectral and MODIS-Aqua-equivalent
 188 $R_{rs}(\lambda)$ data having three DoF, and SeaWiFS-equivalent $R_{rs}(\lambda)$ data having two DoF.
 189 This suggests that there is one DoF in the 651–700nm range that is picked up by hyper-
 190 spectral and multispectral $R_{rs}(\lambda)$ alike; however, the $R_{rs}(\lambda)$ values are small enough (mean
 191 and median both $<1.2 \times 10^{-4} \text{sr}^{-1}$ for all wavelengths 651–700nm) compared to the nominal
 192 1km-by-1km pixel uncertainty $3 \times 10^{-4} \text{sr}^{-1}$) that this DoF may not be useful for
 193 satellite applications, which we are interested in here. This is corroborated by the DoF < 3
 194 in the next section, despite incorporating the full wavebands of both MODIS-Aqua and
 195 SeaWiFS. Note that when estimating the MODIS-Aqua- and SeaWiFS-equivalent data
 196 from 400–650nm hyperspectral data, the contribution of hyperspectral $R_{rs} > 650\text{nm}$
 197 is not included; while both MODIS-Aqua and SeaWiFS have wavebands centered at $>650\text{nm}$,
 198 these wavebands’ spectral response functions are nonzero for some wavelengths in the
 199 range 400–650nm, and it is only the influence of these hyperspectral wavelengths on all
 200 wavebands that is considered. In other words, $R_{rs}(\lambda)$ is effectively set to zero for all hyper-
 201 spectral wavelengths $>650\text{nm}$ when calculating the multispectral equivalent datasets
 202 in this case.
 203

204 3 Climatologies: R_{rs} versus products

205 The analysis in Section 2 is based on instantaneous, local-scale $R_{rs}(\lambda)$ values measured in situ at the sea surface. The power of satellite $R_{rs}(\lambda)$ and derived products, however, lies in their near-continuous global spatial coverage, and many users are primarily interested in climatological data, which is near the coarsest spatial and temporal scales. In this section we therefore analyze climatological $R_{rs}(\lambda)$ and derived products, again via PCA to determine DoF.

211 We generated a $1^\circ \times 1^\circ$ climatology for each month using $R_{rs}(\lambda)$ data from SeaWiFS spanning 1997–2008, excluding the final 2 years of the mission due to known instrument issues (Siegel et al., 2014), using data downloaded from <https://oceancolor.gsfc.nasa.gov/>. We did the same for MODIS-Aqua, spanning the time period from July 2002 – June 2022. We generated analogous climatologies for derived products from each satellite over the same period and at the same spatial and temporal resolution, namely the extensive (i.e. mass-dependent) variables Chl, C_{phyto} , POC, PIC, and the intensive (i.e. mass-independent) variables Z_{eu} , ξ , the fraction of biovolume in the microplankton size class f_{micro} calculated from ξ as described in (Kostadinov et al., 2009), the particulate backscatter to chlorophyll ratio $b_{bp} : \text{Chl}$, and NPP as estimated by the CAFE (Silsbe et al., 2016) and CbPMv2 (Westberry et al., 2008) models. Chl, POC, and PIC were downloaded from <https://oceancolor.gsfc.nasa.gov/>, as was b_{bp} to calculate C_{phyto} according to (Graff et al., 2015) and $b_{bp} : \text{Chl}$ and the diffuse attenuation coefficient at 490nm to calculate Z_{eu} according to (Lee et al., 2007); SeaWiFS ξ and f_{micro} were derived as in (Kostadinov et al., 2009); and NPP products were downloaded from <http://sites.science.oregonstate.edu/ocean.productivity/index.php>. In total we then have climatologies for MODIS-Aqua, SeaWiFS $R_{rs}(\lambda)$, and ten derived products. We consider the six products Chl, C_{phyto} , POC, PIC, ξ , and Z_{eu} , to be core products and f_{micro} , $b_{bp} : \text{Chl}$, CAFE NPP, and CbPMv2 NPP to be ancillary products as these are either derived from the core products or rely on ancillary data other than $R_{rs}(\lambda)$.

231 We note that a PCA on the MODIS-Aqua climatologies of $R_{rs}(\lambda)$ and products other than ξ and f_{micro} yields the same results as those for SeaWiFS below, so we focus here only on the SeaWiFS climatologies because ξ and f_{micro} are not readily available for MODIS-Aqua. We find two DoF for SeaWiFS $R_{rs}(\lambda)$, but only one for the products (Figure 4). This result is not sensitive to which combination of products is used – for instance, including all the ancillary products as well still results in one DoF for the products. This result is also not sensitive to log-transformations of the variables that are log-normally (e.g. Chl, POC, PIC, C_{phyto} (Campbell, 1995)) or log-skew-normally (e.g. NPP, (Cael et al., 2018; Cael, 2021)) distributed, or removal of outliers, zeros, or negative values.

241 That MODIS-Aqua $R_{rs}(\lambda)$ have three DoF for the data in the previous section but two DoF from satellite-derived climatologies suggests that some reduction of complexity of the data occurs via some combination of increased sensor noise relative to ship-based data, atmospheric correction, or averaging over large space and time scales (Scott & Werdell, 2019). (Note (Scott & Werdell, 2019) also point out the difference between averaging $R_{rs}(\lambda)$ versus taking the ratio of averaged water-leaving radiance Lw and downwelling irradiance, which may introduce a slight bias but is unlikely to affect our results here.) Two DoF remain in satellite climatological $R_{rs}(\lambda)$ for both SeaWiFS and MODIS-Aqua, indicating the possibility of generating two independent products from these data. The suite of products tested above, however, has one fewer DoF than the $R_{rs}(\lambda)$. This is likely due to derived products’ appreciable uncertainties and/or strong correlations with chlorophyll. POC, ξ , and Z_{eu} , for instance, have Spearman rank correlations (across all months and 1° grid cells) of >0.9 with Chl. C_{phyto} ’s rank correlation with Chl is still fairly high, at 0.61, and is low largely due to small fluctuations when both are small; a simple spline fit of $\log(C_{phyto})$ against $\log(\text{Chl})$ yields an r^2 of 0.7.

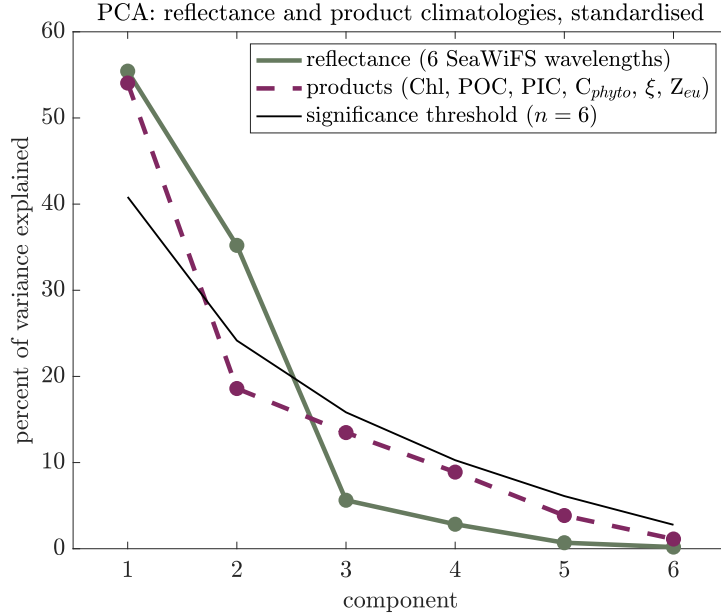


Figure 4. Scree plot of percent variance explained versus component for climatologies of SeaWiFS $R_{rs}(\lambda)$ and of six SeaWiFS- $R_{rs}(\lambda)$ -derived products. Black line indicates broken-stick significance threshold for six-dimensional data.

256 The exception is PIC, which has a rank correlation with Chl of 0.11. PIC, how-
 257 ever, is highly sensitive to small variations in $R_{rs}(\lambda)$ for typical $R_{rs}(\lambda)$ values. To sub-
 258 stantiate this, we performed a simple sensitivity analysis with the standard two-band PIC
 259 algorithm used by NASA for all but the most optically bright waters (see [https://oceancolor](https://oceancolor.gsfc.nasa.gov/atbd/pic/)
 260 [.gsfc.nasa.gov/atbd/pic/](https://oceancolor.gsfc.nasa.gov/atbd/pic/)). We calculated PIC for the climatological median $R_{rs}(\lambda)$
 261 at 443 nm and 555 nm and for 5% variations, converting to normalized water-leaving ra-
 262 diance by multiplying by the global mean extraterrestrial solar irradiance. We then per-
 263 turbed these $R_{rs}(\lambda)$ values with Gaussian noise at the 5% level, corresponding to the
 264 nominal uncertainty in $R_{rs}(\lambda)$. This noise at 443 nm results in 68% noise in PIC. By con-
 265 trast, POC only varies 5% with these 5% variations in $R_{rs}(\lambda)$ at either wavelength. This
 266 indicates that in the bulk of cases, satellite-derived PIC is highly uncertain, on the or-
 267 der of 70% (and note the PIC uncertainty will be magnified more when considering docu-
 268 mented uncertainties for $R_{rs}(\lambda)$ of 15-40% in some regions (Bisson et al., 2021)). In con-
 269 trast, for relatively bright waters, the same exercise resulted in PIC variations of <10%,
 270 indicating that this algorithm performs well in instances when PIC values are high. Nonethe-
 271 less, the high sensitivity to typical uncertainty in $R_{rs}(\lambda)$ for median waters explains why
 272 we find one DoF for the products even though PIC and Chl are not strongly correlated:
 273 derived PIC is noisy most of the time.

274 These results have two key implications. One is that there is additional informa-
 275 tion in climatological $R_{rs}(\lambda)$ that is not included in current derived products. This im-
 276 plies that existing products do not utilize the full set of $R_{rs}(\lambda)$ wavelengths. The other
 277 implication is that these products are not at all independent, and should not be treated
 278 as such when using them simultaneously. In other words, there are more products than
 279 there are DoF in satellite data. A numerical ecosystem model that reproduces the satellite-
 280 derived climatology of chlorophyll and of the particle size distribution’s spectral slope
 281 should not be considered to be capturing two independent properties of the Earth sys-

282 tem. When using satellite products as inputs to other models, these products and their
 283 propagated uncertainties must be treated simultaneously rather than independently.

284 The results presented here are appropriate for global ocean analyses. The open ocean
 285 represents the largest area, and is composed primarily of Case 1 waters; that is, waters
 286 in which optical variability is dominated by chlorophyll (Morel & Prieur, 1977). In this
 287 context, it is in a sense unsurprising that the suite of $R_{rs}(\lambda)$ -derived products produced
 288 only one DoF. More optically complex waters, such as coastal regions and inland waters,
 289 have optical variability that is influenced by other constituents, such as colored dissolved
 290 organic material (CDOM), inorganic particles, and other pigments in addition to chloro-
 291 phyll (e.g. Brown et al., 2008; Nelson & Siegel, 2013)). Analyses focused on these wa-
 292 ters is likely to reveal a higher number of DoF from both $R_{rs}(\lambda)$ and derived products.
 293 Indeed, algorithms to derive concentrations of cyanobacteria and suspended particulate
 294 (Wang et al., 2016)) or distinguish between different phytoplankton species (Erickson
 295 et al., 2020) can be successful in such waters. However, we note that the in situ dataset
 296 used here (Figure 1) represents waters with $R_{rs}(\lambda)$ variability similar to that of the ocean
 297 as a whole, which can be seen by comparing the variation in $R_{rs}(\lambda)$ at each MODIS-Aqua
 298 wavelength from global satellite data with the same satellite data sub-sampled to the lo-
 299 cations with in situ measurements (or the closest non-cloudy location). Sub-sampled satel-
 300 lite measurements have similar, and slightly lower, $R_{rs}(\lambda)$ in bluer wavelengths, indicat-
 301 ing that the in situ dataset is oriented more towards optically complex coastal waters
 302 with substantial CDOM. This suggests that part of the explanation for the drop in DoF
 303 in satellite-derived climatologies comes from the fact that the in situ dataset sampled,
 304 as a whole, more optically complex waters.

305 We find that both $R_{rs}(\lambda)$ and variables derived from $R_{rs}(\lambda)$ are highly inter-correlated,
 306 reducing the number of DoF associated with each, with a greater reduction in DoF in
 307 the derived products. This becomes a problem when products are derived using empir-
 308 ical relationships with $R_{rs}(\lambda)$, and especially when the same wavelengths are used for
 309 the products that are assumed to be independent of each other; for example, over much
 310 of the ocean PIC, POC, and chlorophyll all are functions only of $R_{rs}(\lambda)$ at two wave-
 311 lengths, at (or near, depending on the sensor) 443 and 555 nm. Certain combinations
 312 of PIC, POC, and chlorophyll, which may occur in the surface ocean, are therefore im-
 313 possible to find using these algorithms. This is distinct from algorithms, typically called
 314 “quasi-analytical” or “semi-empirical”, that use known or assumed spectral shapes for
 315 absorption and scattering properties of optical constituents that can be related to the
 316 same derived products, such as PIC, POC, and chlorophyll (Werdell et al., 2013). These
 317 approaches may result in similar correlations and DoF between derived products, but
 318 do not inherently have the same problems as empirical approaches. We note that PACE
 319 will have, in addition to hyperspectral visible bands, UV bands from 350nm as well as
 320 spectral polarized bands. These measurements are expected to both improve the atmo-
 321 spheric correction (hence reduce the $R_{rs}(\lambda)$ uncertainties) as well as provide their own
 322 ocean signals, both of which may increase the DoF compared to those found here. In ad-
 323 dition, it has been shown that adding other environmental variables such as SST can add
 324 useful information to inversions of phytoplankton groups (e.g. Chase et al., 2022) and
 325 thus another approach to increase DoF for inversions by adding relevant and indepen-
 326 dent information (e.g. mixed-layer depth and nutrients from BGC-Argo assimilating mod-
 327 els).

328 4 Conclusion

329 The results presented here highlight the high degree of co-dependence between re-
 330 mote sensing reflectances at different wavelengths and of the products derived from these
 331 reflectances. For users of products based on existing reflectances, this primarily means
 332 factoring in the relationships between products when using more than one simultane-
 333 ously. For the algorithms that generate these products from existing reflectances, these

334 results indicate a potential to improve the suite of available products to be more accu-
335 rate and precise, and to account for the relationships between products and $R_{rs}(\lambda)$ wave-
336 bands. One way to do this, consistent with the findings above, would be to derive a sin-
337 gular product such as chlorophyll as a function of all reflectance wavebands, derive an anomaly
338 from chlorophyll-based expectations of a secondary product (e.g., phytoplankton com-
339 munity composition, size, POC, PIC, and so forth), then specify all other products ex-
340 plicitly as a function of these two, along the lines of Alvain et al. (2005). Ancillary and
341 independent information can also be added to algorithms, as is currently done with net
342 primary production models via temperature and mixed layer depth.

343 These findings are most relevant for algorithms that will generate products from
344 hyperspectral reflectances in the future. The small number of degrees of freedom in hy-
345 perspectral reflectances indicates that only a few quantities can be estimated independ-
346 dently, and that different wavelengths' reflectances as measured from space will be strongly
347 correlated. Complex algorithms that utilize the full spectrum of reflectance will need to
348 factor in these correlations in order to generate reliable products. Crucially, if more than
349 a few products are generated from hyperspectral reflectances, as is likely the case, such
350 algorithms will also need to output the covariance information encoding the uncertainty
351 in each product and the relationships between them. This can be achieved by some, but
352 not all, machine learning techniques, on which this new generation of algorithms are likely
353 to be based. The fact that hyperspectral reflectances can be predicted within nominal
354 uncertainties by their multispectral equivalents suggests that hyperspectral resolution
355 can play a role in improving ocean color products, but that it will be challenging to pro-
356 vide a substantially finer-grained picture of surface ocean ecosystems and biogeochem-
357 ical cycles. Here by relying on principal component analysis we have focused on broad,
358 first-order variations, but where such resolution may be most useful and generate novel
359 insights is in investigating outliers and rare events, such as blooms or binning data over
360 coherent features like eddies, where e.g. monospecific signatures may be resolved with
361 spectral precision.

362 Open Research

363 Remote sensing data were downloaded from <https://oceancolor.gsfc.nasa.gov/>
364 and <http://sites.science.oregonstate.edu/ocean.productivity/index.php>. All
365 data and code are available at github.com/bbcael/eifoc for review purposes and will
366 be given a Zenodo DOI should this manuscript be accepted for publication.

367 Acknowledgments

368 It is a pleasure to thank the many scientists whose collective work has generated the data
369 on which this work relies. Cael acknowledges support from the National Environmen-
370 tal Research Council through Enhancing Climate Observations, Models and Data, and
371 the European Union's Horizon 2020 Research and Innovation Programme under grant
372 agreement No. 820989 (project COMFORT). The work reflects only the authors' view;
373 the European Commission and their executive agency are not responsible for any use that
374 may be made of the information the work contains. KB acknowledges support from NASA
375 grant 80NSSC18K0957. EB acknowledges support from NASA grant 80NSSC20M0203.
376 Cael lead and all other authors assisted with all aspects of this work. The authors have
377 no competing interests to declare. This is PMEL contribution number 5445.

378 References

379 Alvain, S., Moulin, C., Dandonneau, Y., & Breon, F.-M. (2005). Remote sensing of
380 phytoplankton groups in case 1 waters from global seawifs imagery. *Deep Sea*
381 *Research Part I: Oceanographic Research Papers*, 52(11), 1989–2004.

- 382 Behrenfeld, M. J., & Falkowski, P. G. (1997). Photosynthetic rates derived from
 383 satellite-based chlorophyll concentration. *Limnology and oceanography*, *42*(1),
 384 1–20.
- 385 Bisson, K., Boss, E., Werdell, P. J., Ibrahim, A., Fouin, R., & Behrenfeld, M.
 386 (2021). Seasonal bias in global ocean color observations. *Applied optics*,
 387 *60*(23), 6978–6988.
- 388 Bisson, K., Siegel, D. A., & DeVries, T. (2020). Diagnosing mechanisms of ocean
 389 carbon export in a satellite-based food web model. *Frontiers in Marine Sci-*
 390 *ence*, *7*, 505.
- 391 Brown, C. A., Huot, Y., Werdell, P. J., Gentili, B., & Claustre, H. (2008). The
 392 origin and global distribution of second order variability in satellite ocean
 393 color and its potential applications to algorithm development. *Remote*
 394 *Sensing of Environment*, *112*(12), 4186–4203. Retrieved from [https://](https://www.sciencedirect.com/science/article/pii/S0034425708002162)
 395 www.sciencedirect.com/science/article/pii/S0034425708002162 doi:
 396 <https://doi.org/10.1016/j.rse.2008.06.008>
- 397 Cael, B. (2021). Variability-based constraint on ocean primary production models.
 398 *Limnology and Oceanography Letters*, *6*(5), 262–269.
- 399 Cael, B., Bisson, K., & Follett, C. L. (2018). Can rates of ocean primary production
 400 and biological carbon export be related through their probability distributions?
 401 *Global biogeochemical cycles*, *32*(6), 954–970.
- 402 Cael, B., Bisson, K., & Follows, M. J. (2017). How have recent temperature changes
 403 affected the efficiency of ocean biological carbon export? *Limnology and*
 404 *Oceanography Letters*, *2*(4), 113–118.
- 405 Cael, B., Chase, A., & Boss, E. (2020). Information content of absorption spectra
 406 and implications for ocean color inversion. *Applied Optics*, *59*(13), 3971–3984.
- 407 Cael, B., Dutkiewicz, S., & Henson, S. (2021). Abrupt shifts in 21st-century plank-
 408 ton communities. *Science advances*, *7*(44), eabf8593.
- 409 Campbell, J. W. (1995). The lognormal distribution as a model for bio-optical vari-
 410 ability in the sea. *Journal of Geophysical Research: Oceans*, *100*(C7), 13237–
 411 13254.
- 412 Chase, A. P., Boss, E., Cetinić, I., & Slade, W. (2017). Estimation of phytoplankton
 413 accessory pigments from hyperspectral reflectance spectra: toward a global
 414 algorithm. *Journal of Geophysical Research: Oceans*, *122*(12), 9725–9743.
- 415 Chase, A. P., Boss, E. S., Haëntjens, N., Culhane, E., Roesler, C., & Karp-Boss,
 416 L. (2022). Plankton imagery data inform satellite-based estimates of diatom
 417 carbon. *Geophysical Research Letters*, *49*(13), e2022GL098076. Retrieved
 418 from [https://agupubs.onlinelibrary.wiley.com/doi/abs/10.1029/](https://agupubs.onlinelibrary.wiley.com/doi/abs/10.1029/2022GL098076)
 419 [2022GL098076](https://agupubs.onlinelibrary.wiley.com/doi/abs/10.1029/2022GL098076) (e2022GL098076 2022GL098076) doi: [https://doi.org/10.1029/](https://doi.org/10.1029/2022GL098076)
 420 [2022GL098076](https://doi.org/10.1029/2022GL098076)
- 421 DeVries, T., & Weber, T. (2017). The export and fate of organic matter in the
 422 ocean: New constraints from combining satellite and oceanographic tracer
 423 observations. *Global Biogeochemical Cycles*, *31*(3), 535–555.
- 424 Dutkiewicz, S., Cermeno, P., Jahn, O., Follows, M. J., Hickman, A. E., Taniguchi,
 425 D. A., & Ward, B. A. (2020). Dimensions of marine phytoplankton diversity.
 426 *Biogeosciences*, *17*(3), 609–634.
- 427 Erickson, Z. K., Werdell, P. J., & Cetinić, I. (2020). Bayesian retrieval of optically
 428 relevant properties from hyperspectral water-leaving reflectances. *Applied Op-*
 429 *tics*, *59*(23), 6902–6917. doi: 10.1364/AO.398043
- 430 Evers-King, H., Martinez-Vicente, V., Brewin, R. J., Dall’Olmo, G., Hickman, A. E.,
 431 Jackson, T., ... others (2017). Validation and intercomparison of ocean color
 432 algorithms for estimating particulate organic carbon in the oceans. *Frontiers*
 433 *in Marine Science*, 251.
- 434 Gordon, H. R., & Wang, M. (1994). Retrieval of water-leaving radiance and aerosol
 435 optical thickness over the oceans with seawifs: a preliminary algorithm. *Ap-*
 436 *plied optics*, *33*(3), 443–452.

- 437 Graff, J. R., Westberry, T. K., Milligan, A. J., Brown, M. B., Dall’Olmo, G., van
438 Dongen-Vogels, V., . . . Behrenfeld, M. J. (2015). Analytical phytoplankton
439 carbon measurements spanning diverse ecosystems. *Deep Sea Research Part I:
440 Oceanographic Research Papers*, *102*, 16–25.
- 441 Hovis, W. A., Clark, D., Anderson, F., Austin, R., Wilson, W., Baker, E., . . . others
442 (1980). Nimbus-7 coastal zone color scanner: system description and initial
443 imagery. *Science*, *210*(4465), 60–63.
- 444 Hu, C., Lee, Z., & Franz, B. (2012). Chlorophyll algorithms for oligotrophic oceans:
445 A novel approach based on three-band reflectance difference. *Journal of Geo-
446 physical Research: Oceans*, *117*(C1).
- 447 Huot, Y., & Antoine, D. (2016). Remote sensing reflectance anomalies in the ocean.
448 *Remote Sensing of Environment*, *184*, 101–111. doi: 10.1016/j.rse.2016.06.002
- 449 Jackson, D. A. (1993). Stopping rules in principal components analysis: a compari-
450 son of heuristical and statistical approaches. *Ecology*, *74*(8), 2204–2214.
- 451 Kostadinov, T., Siegel, D., & Maritorena, S. (2009). Retrieval of the particle size
452 distribution from satellite ocean color observations. *Journal of Geophysical Re-
453 search: Oceans*, *114*(C9).
- 454 Kramer, S. J., Siegel, D. A., Maritorena, S., & Catlett, D. (2022). Modeling surface
455 ocean phytoplankton pigments from hyperspectral remote sensing reflectance
456 on global scales. *Remote Sensing of Environment*, *270*, 112879.
- 457 Lee, Z., Weidemann, A., Kindle, J., Arnone, R., Carder, K. L., & Davis, C. (2007).
458 Euphotic zone depth: Its derivation and implication to ocean-color remote
459 sensing. *Journal of Geophysical Research: Oceans*, *112*(C3).
- 460 Mitchell, C., Hu, C., Bowler, B., Drapeau, D., & Balch, W. (2017). Estimating par-
461 ticulate inorganic carbon concentrations of the global ocean from ocean color
462 measurements using a reflectance difference approach. *Journal of Geophysical
463 Research: Oceans*, *122*(11), 8707–8720.
- 464 Morel, A., & Prieur, L. (1977). Analysis of variations in ocean color 1. *Limnology
465 and oceanography*, *22*(4), 709–722.
- 466 Nelson, N. B., & Siegel, D. A. (2013). The global distribution and dynamics of chro-
467 mophoric dissolved organic matter. *Annual review of marine science*, *5*, 447–
468 476.
- 469 Nowicki, M., DeVries, T., & Siegel, D. A. (2022). Quantifying the carbon export and
470 sequestration pathways of the ocean’s biological carbon pump. *Global Biogeo-
471 chemical Cycles*, *36*(3), e2021GB007083.
- 472 O’Reilly, J. E., Maritorena, S., Mitchell, B. G., Siegel, D. A., Carder, K. L., Garver,
473 S. A., . . . McClain, C. (1998). Ocean color chlorophyll algorithms for seawifs.
474 *Journal of Geophysical Research: Oceans*, *103*(C11), 24937–24953.
- 475 Scholz, M., Fraunholz, M., & Selbig, J. (2008). Nonlinear principal component anal-
476 ysis: neural network models and applications. In *Principal manifolds for data
477 visualization and dimension reduction* (pp. 44–67). Springer.
- 478 Scott, J. P., & Werdell, P. J. (2019). Comparing level-2 and level-3 satellite ocean
479 color retrieval validation methodologies. *Optics Express*, *27*(21), 30140–30157.
- 480 Siegel, D., Buesseler, K., Doney, S. C., Sailley, S., Behrenfeld, M. J., & Boyd, P.
481 (2014). Global assessment of ocean carbon export by combining satellite obser-
482 vations and food-web models. *Global Biogeochemical Cycles*, *28*(3), 181–196.
- 483 Silsbe, G. M., Behrenfeld, M. J., Halsey, K. H., Milligan, A. J., & Westberry, T. K.
484 (2016). The cafe model: A net production model for global ocean phytoplankton.
485 *Global Biogeochemical Cycles*, *30*(12), 1756–1777.
- 486 Wang, G., Lee, Z., Mishra, D. R., & Ma, R. (2016). Retrieving absorption coef-
487 ficients of multiple phytoplankton pigments from hyperspectral remote sens-
488 ing reflectance measured over cyanobacteria bloom waters. *Limnology and
489 Oceanography: Methods*, *14*(7), 432–447. doi: 10.1002/lom3.10102
- 490 Weinberger, K. Q., Sha, F., & Saul, L. K. (2004). Learning a kernel matrix for non-
491 linear dimensionality reduction. In *Proceedings of the twenty-first international*

- 492 *conference on machine learning* (p. 106).
- 493 Werdell, P. J., Behrenfeld, M. J., Bontempi, P. S., Boss, E., Cairns, B., Davis,
494 G. T., ... others (2019). The plankton, aerosol, cloud, ocean ecosystem
495 mission: status, science, advances. *Bulletin of the American Meteorological*
496 *Society*, 100(9), 1775–1794.
- 497 Werdell, P. J., Franz, B. A., Bailey, S. W., Feldman, G. C., Boss, E., Brando, V. E.,
498 ... others (2013). Generalized ocean color inversion model for retrieving
499 marine inherent optical properties. *Applied Optics*, 52(10), 2019–2037.
- 500 Westberry, T., Behrenfeld, M., Siegel, D., & Boss, E. (2008). Carbon-based primary
501 productivity modeling with vertically resolved photoacclimation. *Global Bio-*
502 *geochemical Cycles*, 22(2).
- 503 Wold, S., Esbensen, K., & Geladi, P. (1987). Principal component analysis. *Chemo-*
504 *metrics and intelligent laboratory systems*, 2(1-3), 37–52.

Extracting information from ocean color

B. B. Cael¹, Kelsey Bisson², Emmanuel Boss³, and Zachary K. Erickson⁴

¹National Oceanography Centre, Southampton, UK

²Oregon State University, Corvallis, OR, USA

³University of Maine, Orono, ME, USA

⁴NOAA Pacific Marine Environmental Laboratory, Seattle, WA, USA

Key Points:

- In situ hyperspectral $R_{rs}(400-700\text{nm})$ have 4 degrees of freedom & are predicted within uncertainties by MODIS & SeaWiFS wavebands.
- Degrees of freedom are lost upscaling to global satellite climatologies and again to $R_{rs}(\lambda)$ -derived products like chlorophyll.
- Information exists in satellite $R_{rs}(\lambda)$ that's underutilized by products' algorithms. Future algorithms must consider correlations carefully.

Corresponding author: B. B. Cael, cael@noc.ac.uk

Abstract

Products derived from remote sensing reflectances ($R_{rs}(\lambda)$), e.g. chlorophyll, phytoplankton carbon, euphotic depth, or particle size, are widely used in oceanography. Problematically, $R_{rs}(\lambda)$ may have fewer degrees of freedom (DoF) than measured wavebands or derived products. A global sea surface hyperspectral $R_{rs}(\lambda)$ dataset has DoF=4. MODIS-like multispectral equivalent data also have DoF=4, while their SeaWiFS equivalent has DoF=3. Both multispectral-equivalent datasets predict individual hyperspectral wavelengths' $R_{rs}(\lambda)$ within nominal uncertainties. Remotely sensed climatological multispectral $R_{rs}(\lambda)$ have DoF=2, as information is lost by atmospheric correction, shifting to larger spatiotemporal scales, and/or more open-ocean measurements, but suites of $R_{rs}(\lambda)$ -derived products have DoF=1. These results suggest that remote sensing products based on existing satellites' $R_{rs}(\lambda)$ are not independent and should not be treated as such, that existing $R_{rs}(\lambda)$ measurements hold unutilized information, and that future multi- or especially hyper-spectral algorithms must rigorously consider correlations between $R_{rs}(\lambda)$ wavebands.

Plain Language Summary

The reflectance of sunlight from the ocean can be observed from satellites and is used to derive many biologically-relevant parameters, such as the concentration of chlorophyll in the upper ocean. Reflectances are currently observed at about ten different wavelengths, but this will soon be expanded to hundreds with the upcoming launch of a new ocean color satellite, PACE, in early 2024. Many new algorithms are being proposed to make use of the wealth of ocean color data which will be provided. However, there are strong correlations between reflectances at different wavelengths; these correlations mean there will be far fewer products that can be independently derived than there will be reflectance wavelengths observed. Here we use a ship-based measurements similar to what will be provided from PACE to suggest that, on a global scale, only a few independent variables can be calculated from hundreds of reflectance wavelengths. Current and past satellites provide a similar amount of independent data to what is projected from PACE. We then show that, on a global scale, a set of six derived parameters only contains one independent piece of information, suggesting that more information exists in ocean color data than is being currently used.

1 Introduction

Ocean color satellites have revolutionized the study of ocean ecology and biogeochemistry in recent decades by providing a near-continuous global picture of surface ocean properties (Hovis et al., 1980; O'Reilly et al., 1998). Satellites measure the spectral radiance emanating from the ocean and atmosphere. Remote sensing reflectance ($R_{rs}(\lambda)$) is obtained following the removal of the contribution of atmospheric and surface effects and normalization to downwelling solar irradiance. Algorithms have been developed to estimate numerous biogeochemically-relevant surface variables from $R_{rs}(\lambda)$, such as chlorophyll concentration (Chl, [$\mu\text{g/L}$]) (O'Reilly et al., 1998; Hu et al., 2012), the spectral slope of the particle size distribution (ξ) (Kostadinov et al., 2009), the concentrations of phytoplankton and particulate organic and inorganic carbon (C_{phyto} , POC, and PIC, [$\mu\text{g/L}$]) (Graff et al., 2015; Evers-King et al., 2017; Mitchell et al., 2017), euphotic layer depth (Z_{eu} [m]) (Lee et al., 2007), and, using additional input variables, net primary production (NPP, [$\text{mg/m}^2\text{d}$]) (Behrenfeld & Falkowski, 1997; Silsbe et al., 2016; Westberry et al., 2008). Such products are used in a wide variety of applications, such as validation of complex ocean ecosystem and biogeochemistry models (Dutkiewicz et al., 2020; Cael et al., 2021) or as inputs for simpler models that predict other variables such as vertical particulate organic carbon fluxes from ocean color (Siegel et al., 2014; Cael et al., 2017; DeVries & Weber, 2017; Nowicki et al., 2022; Bisson et al., 2020).

Existing $R_{rs}(\lambda)$ data are multispectral, meaning they are measured within several individually determined wavebands. Derived products generally rely only on a subset of these wavebands and are commonly expressed as functions of band ratios between just two wavelengths (e.g. Hu et al., 2012). Some algorithms attempt to simultaneously estimate multiple products to match the full spectrum of $R_{rs}(\lambda)$; for example, the Generalized Inherent Optical Properties (GIOP) approach (Werdell et al., 2013) uses known and assumed spectral shapes of backscattering and absorption from different optical constituents to estimate the suite of products that best represents the observed $R_{rs}(\lambda)$. However, the most widely used products, such as for Chl and POC, treat all outputs as independent quantities and are fully empirical.

Correlations between $R_{rs}(\lambda)$ at different wavebands can be quite strong (Huot & Antoine, 2016), depending also on the spatiotemporal scales considered (see §3). This presents multiple potential issues for both users and developers of ocean color derived products. If multiple products are used simultaneously and treated as independent when they are in fact not, this can lead to overconfidence in model skill or miscalculation of uncertainties. An unintended consequence of treating satellite products independently within models is a functional limit on model complexity. Adding different (yet correlated) satellite products to a model can result in model output redundancy (Bisson et al., 2020). These issues will only be exacerbated by the hyperspectral resolution of the next generation of ocean color satellites, namely the Plankton, Clouds, Aerosols and Ecosystems (PACE) satellite scheduled to launch January 2024 (Werdell et al., 2019). In addition to the common suite of multispectral products, PACE also plans to move beyond chlorophyll and enable characterizations of phytoplankton communities (e.g. Chase et al., 2017), substantially increasing the number of products available from $R_{rs}(\lambda)$.

The strong correlations among $R_{rs}(\lambda)$ wavelengths can be framed in terms of the degrees of freedom (DoF) of $R_{rs}(\lambda)$ measurements and suites of derived products. DoF represents the effective number of dimensions of a dataset after accounting for correlations and uncertainties between variables and is in essence the number of independent variables in that dataset. It has been shown that the DoF of globally distributed near-surface measured hyperspectral absorption spectra is about five (Cael et al., 2020). This could be considered a possible upper limit for the DoF of satellite-measured $R_{rs}(\lambda)$ given higher uncertainties on satellite measurements – particularly associated with atmospheric correction (Bisson et al., 2021; Cael et al., 2020). The DoF of PACE’s hyperspectral measurements might then be expected to be much lower than the number of wavelengths for which it will measure $R_{rs}(\lambda)$, which will appreciably affect how hyperspectral satellite $R_{rs}(\lambda)$ products should be constructed. For both existing and future satellite $R_{rs}(\lambda)$, in other words, understanding the DoF of $R_{rs}(\lambda)$ measurements and derived products is crucial for appropriate usage and optimal construction of such products.

Here we investigate the DoF of $R_{rs}(\lambda)$. We first find that a global sea surface hyperspectral $R_{rs}(\lambda)$ database has four DoF. Coarsening hyperspectral $R_{rs}(\lambda)$ to their MODIS (Moderate Resolution Imaging Spectrometer) equivalent retains four DoF, though the SeaWiFS (Sea-viewing Wide Field of view Sensor) equivalent only has three DoF. Both of these multispectral equivalents can, however, predict individual hyperspectral $R_{rs}(\lambda)$ wavelengths within nominal uncertainties for satellite sensors. We then consider climatological $R_{rs}(\lambda)$ and derived products. We find that both MODIS-Aqua and SeaWiFS $R_{rs}(\lambda)$ have two DoF at the climatological scale, suggesting that $R_{rs}(\lambda)$ complexity is lost either through atmospheric correction, relatively more inclusion of open-ocean data, or averaging over larger scales in space and time. Suites of derived products, however, only retain one DoF. This latter result suggests that derived products should not be treated as independent by users. We close by discussing the substantial implications these findings have for the construction and use of ocean color products, from both existing and future $R_{rs}(\lambda)$.

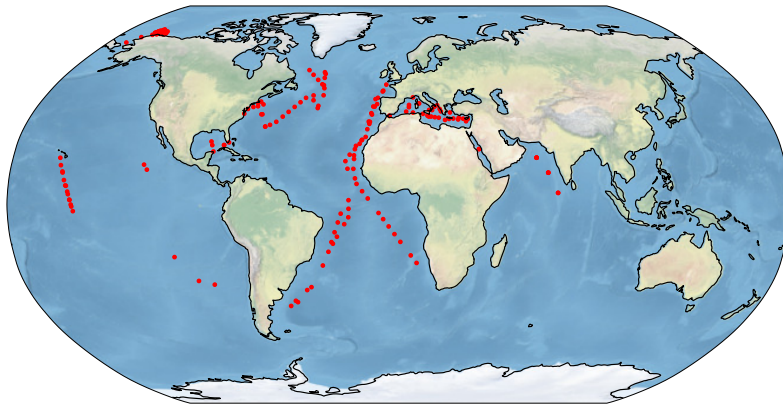


Figure 1. Locations of the 191 stations considered in this study (red dots).

116

2 Sea surface R_{rs} : hyperspectral versus multispectral

117

118

119

120

121

122

123

124

125

126

127

128

129

130

131

132

We first analyze a global sea surface hyperspectral $R_{rs}(\lambda)$ dataset to determine its DoF and how the DoF depends on spectral resolution (Chase et al., 2017; Kramer et al., 2022). The dataset includes $R_{rs}(\lambda)$ data at 191 locations at an effective 3.35 nm resolution (Chase et al., 2017) from 400–800 nm, linearly interpolated to 1 nm (Figure 1). We trimmed spectra to 700nm due to the large fraction of missing values $>700\text{nm}$; note that most of the non-empty values $>700\text{nm}$ are zeros and the non-zero-non-empty values, with a median of $<4 \times 10^{-5} \text{ sr}^{-1}$, have very small signal-to-noise ratios. The dataset includes measurements taken from 2004 to 2018 evenly distributed across months of the year, and from all major ocean basins ranging in latitude from 41°S to 74°N . We also compare these data to their MODIS-Aqua and SeaWiFS multispectral equivalents by convoluting the hyperspectral $R_{rs}(\lambda)$ with the MODIS-Aqua and SeaWiFS spectral response functions (available at https://oceancolor.gsfc.nasa.gov/docs/rsr/HMODISA_RSRs.txt and https://oceancolor.gsfc.nasa.gov/docs/rsr/SeaWiFS_RSRs.txt) to generate 10-waveband and 6-waveband datasets which correspond to what each instrument would have measured from the same optical input that the radiometer received when generating the hyperspectral $R_{rs}(\lambda)$ data.

133

134

135

136

137

138

139

140

141

142

143

144

145

146

147

148

149

150

151

We then apply principal component analysis (PCA) (Wold et al., 1987) to these 301-, 10- and 6-dimensional $R_{rs}(\lambda)$ datasets. PCA is a widely used method to reduce the dimensionality of datasets by identifying orthogonal vectors that explain the most variance in the data. PCA is linear in nature, which may result in an overestimation of effective dimensions by poorly approximating non-linear relationships between variables (e.g. a PCA performed on the pair (x, y) where $y = x^2$ will yield two DoF). Nonlinear generalizations do exist (Weinberger et al., 2004; Scholz et al., 2008), though these are less widely applied due to their additional complexity and computational requirements that make interpretation challenging. One may therefore consider the DoF we report to be upper bounds. We perform a PCA on each $R_{rs}(\lambda)$ dataset, standardizing each first by subtracting from each waveband its mean and then dividing by its standard deviation. This results in a percentage of total variance explained by each component. We use the broken-stick rule to choose the DoF, which states that the DoF is equal to the number of components that explain more variance than would be expected by randomly distributed data; this method was shown to be more consistent than a suite of others in a comparison (Jackson, 1993). These results can be shown visually as a ‘scree’ plot, which plots the percentage of variance explained by each component and for randomly distributed data; the DoF is the number of components with a higher percentage of variance explained than would be expected for randomly distributed data. Our figures also visibly demon-

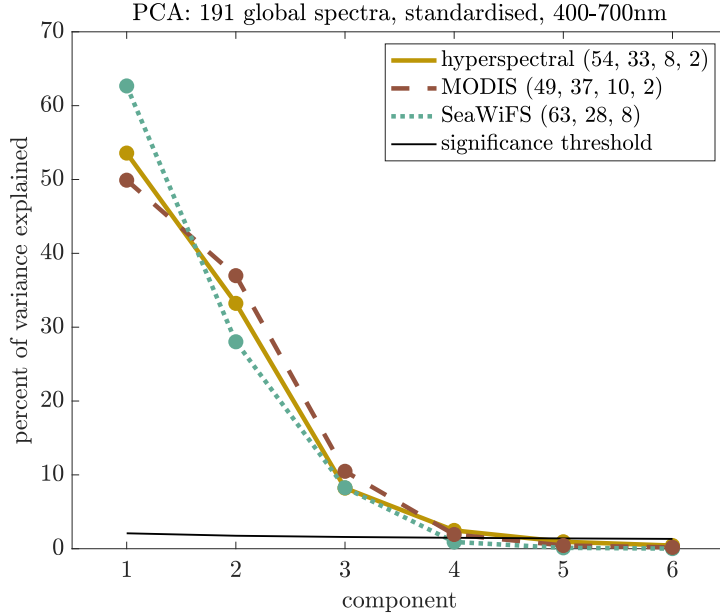


Figure 2. Scree plot of percent variance explained versus component for hyperspectral $R_{rs}(\lambda)$ dataset and MODIS-Aqua and SeaWiFS equivalents calculated from their spectral response functions. Black line indicates broken-stick significance threshold for hyperspectral data; numbers in legend give percent variance explained for each mode above this threshold in each case.

152 strate that one would get the same results from using the scree plot rule, which states
 153 that the DoF is equal to the number of components not sitting on the straight line made
 154 by the higher-order components, and was found to consistently capture the correct DoF
 155 plus one when the first point on this straight line was included (Jackson, 1993).

156 PCA analysis reveals that the hyperspectral in situ $R_{rs}(\lambda)$ dataset has four DoF
 157 (Figure 2); the first four components explain 54%, 33%, 8%, and 2%, totalling 97%, of
 158 the variance. The first four MODIS-Aqua equivalent $R_{rs}(\lambda)$ principal components have
 159 very similar percentages of variance explained: 49%, 37%, 10%, and 2%, totalling 99%
 160 of the total variance. In contrast, the first three SeaWiFS equivalent $R_{rs}(\lambda)$ principal
 161 components explain 63%, 28%, and 8%, totalling 99%, of the variance. This suggests
 162 that the hyperspectral $R_{rs}(\lambda)$ have four DoF, or four independent variables within the
 163 data, and that these four variables are effectively captured when reducing spectral res-
 164 olution to the ten MODIS-Aqua wavebands, but not to the six SeaWiFS wavebands.

165 The ability of coarsened, MODIS-equivalent data to obtain the same number of DoF
 166 as the hyperspectral dataset is further supported by predictions of hyperspectral $R_{rs}(\lambda)$
 167 from multispectral equivalents. To illustrate this, for each hyperspectral wavelength we
 168 perform a multivariate linear regression of $R_{rs}(\lambda)$ at that wavelength regressed against
 169 $R_{rs}(\lambda)$ at each waveband of both the MODIS-Aqua and SeaWiFS equivalent $R_{rs}(\lambda)$. We
 170 then calculate the root-mean-square-error (RMSE) of these regressions. For all wavelengths
 171 below 578 nm in the SeaWiFS case and 582 nm in the MODIS-Aqua case, the RMSE
 172 is smaller – and for many, much smaller – than 5% of the mean $R_{rs}(\lambda)$ at that wavelength,
 173 where 5% is a nominal relative uncertainty for satellite $R_{rs}(\lambda)$ (Figure 3). Even for wave-
 174 lengths greater than this, the RMSE is still very small in absolute terms, $<0.00007 \text{ sr}^{-1}$,
 175 far smaller than the nominal 0.0003 sr^{-1} absolute error for 1km-by-1km pixels for PACE
 176 (Gordon & Wang, 1994). These small errors in predicting hyperspectral $R_{rs}(\lambda)$ from its
 177 multispectral equivalent underscore the extent to which different wavelengths’ $R_{rs}(\lambda)$

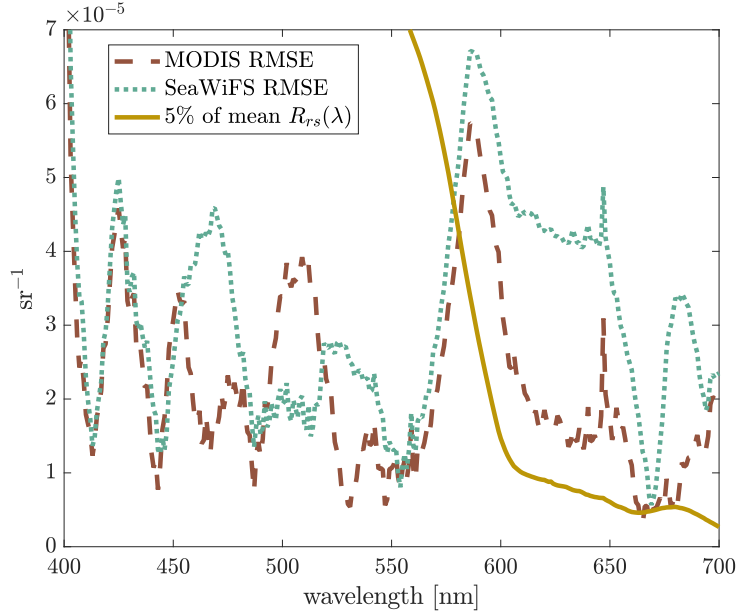


Figure 3. Root-mean-square-error of multivariate linear regressions of each hyperspectral wavelength versus the MODIS-Aqua and SeaWiFS equivalent $R_{rs}(\lambda)$. Solid line is 5% of the mean of each wavelength’s hyperspectral $R_{rs}(\lambda)$.

178 are correlated and demonstrate the ability of MODIS-Aqua equivalent multispectral $R_{rs}(\lambda)$
 179 to preserve the dimensionality of hyperspectral $R_{rs}(\lambda)$. The fact that SeaWiFS-like $R_{rs}(\lambda)$
 180 can accurately predict hyperspectral $R_{rs}(\lambda)$ to within PACE uncertainties but has fewer
 181 DoF than the in situ hyperspectral dataset is a reflection of the lower uncertainty on the
 182 in situ dataset than the expected PACE $R_{rs}(\lambda)$, and suggests that PACE $R_{rs}(\lambda)$ may
 183 have fewer DoF than the in situ hyperspectral dataset.

184 We also note that excluding wavelengths 651–700nm affects the DoF numbers presented here but not our conclusions. A choice of an upper limit of 650nm would be based
 185 on the fact that for all wavelengths above 648nm, >95% of measurements are below 0.0003
 186 sr^{-1} , the nominal uncertainty of a 1km-by-1km pixel for PACE (Gordon & Wang, 1994).
 187 Repeating this analysis over 400–650nm results in hyperspectral and MODIS-Aqua-equivalent
 188 $R_{rs}(\lambda)$ data having three DoF, and SeaWiFS-equivalent $R_{rs}(\lambda)$ data having two DoF.
 189 This suggests that there is one DoF in the 651–700nm range that is picked up by hyper-
 190 spectral and multispectral $R_{rs}(\lambda)$ alike; however, the $R_{rs}(\lambda)$ values are small enough (mean
 191 and median both $<1.2 \times 10^{-4} \text{ sr}^{-1}$ for all wavelengths 651–700nm) compared to the nomi-
 192 nal 1km-by-1km pixel uncertainty $3 \times 10^{-4} \text{ sr}^{-1}$) that this DoF may not be useful for
 193 satellite applications, which we are interested in here. This is corroborated by the DoF < 3
 194 in the next section, despite incorporating the full wavebands of both MODIS-Aqua and
 195 SeaWiFS. Note that when estimating the MODIS-Aqua- and SeaWiFS-equivalent data
 196 from 400–650nm hyperspectral data, the contribution of hyperspectral $R_{rs} > 650\text{nm}$
 197 is not included; while both MODIS-Aqua and SeaWiFS have wavebands centered at $>650\text{nm}$,
 198 these wavebands’ spectral response functions are nonzero for some wavelengths in the
 199 range 400–650nm, and it is only the influence of these hyperspectral wavelengths on all
 200 wavebands that is considered. In other words, $R_{rs}(\lambda)$ is effectively set to zero for all hy-
 201 perspectral wavelengths $>650\text{nm}$ when calculating the multispectral equivalent datasets
 202 in this case.
 203

204 3 Climatologies: R_{rs} versus products

205 The analysis in Section 2 is based on instantaneous, local-scale $R_{rs}(\lambda)$ values measured in situ at the sea surface. The power of satellite $R_{rs}(\lambda)$ and derived products, however, lies in their near-continuous global spatial coverage, and many users are primarily interested in climatological data, which is near the coarsest spatial and temporal scales. In this section we therefore analyze climatological $R_{rs}(\lambda)$ and derived products, again via PCA to determine DoF.

211 We generated a $1^\circ \times 1^\circ$ climatology for each month using $R_{rs}(\lambda)$ data from SeaWiFS spanning 1997–2008, excluding the final 2 years of the mission due to known instrument issues (Siegel et al., 2014), using data downloaded from <https://oceancolor.gsfc.nasa.gov/>. We did the same for MODIS-Aqua, spanning the time period from July 2002 – June 2022. We generated analogous climatologies for derived products from each satellite over the same period and at the same spatial and temporal resolution, namely the extensive (i.e. mass-dependent) variables Chl, C_{phyto} , POC, PIC, and the intensive (i.e. mass-independent) variables Z_{eu} , ξ , the fraction of biovolume in the microplankton size class f_{micro} calculated from ξ as described in (Kostadinov et al., 2009), the particulate backscatter to chlorophyll ratio $b_{bp} : \text{Chl}$, and NPP as estimated by the CAFE (Silsbe et al., 2016) and CbPMv2 (Westberry et al., 2008) models. Chl, POC, and PIC were downloaded from <https://oceancolor.gsfc.nasa.gov/>, as was b_{bp} to calculate C_{phyto} according to (Graff et al., 2015) and $b_{bp} : \text{Chl}$ and the diffuse attenuation coefficient at 490nm to calculate Z_{eu} according to (Lee et al., 2007); SeaWiFS ξ and f_{micro} were derived as in (Kostadinov et al., 2009); and NPP products were downloaded from <http://sites.science.oregonstate.edu/ocean.productivity/index.php>. In total we then have climatologies for MODIS-Aqua, SeaWiFS $R_{rs}(\lambda)$, and ten derived products. We consider the six products Chl, C_{phyto} , POC, PIC, ξ , and Z_{eu} , to be core products and f_{micro} , $b_{bp} : \text{Chl}$, CAFE NPP, and CbPMv2 NPP to be ancillary products as these are either derived from the core products or rely on ancillary data other than $R_{rs}(\lambda)$.

231 We note that a PCA on the MODIS-Aqua climatologies of $R_{rs}(\lambda)$ and products other than ξ and f_{micro} yields the same results as those for SeaWiFS below, so we focus here only on the SeaWiFS climatologies because ξ and f_{micro} are not readily available for MODIS-Aqua. We find two DoF for SeaWiFS $R_{rs}(\lambda)$, but only one for the products (Figure 4). This result is not sensitive to which combination of products is used – for instance, including all the ancillary products as well still results in one DoF for the products. This result is also not sensitive to log-transformations of the variables that are log-normally (e.g. Chl, POC, PIC, C_{phyto} (Campbell, 1995)) or log-skew-normally (e.g. NPP, (Cael et al., 2018; Cael, 2021)) distributed, or removal of outliers, zeros, or negative values.

241 That MODIS-Aqua $R_{rs}(\lambda)$ have three DoF for the data in the previous section but two DoF from satellite-derived climatologies suggests that some reduction of complexity of the data occurs via some combination of increased sensor noise relative to ship-based data, atmospheric correction, or averaging over large space and time scales (Scott & Werdell, 2019). (Note (Scott & Werdell, 2019) also point out the difference between averaging $R_{rs}(\lambda)$ versus taking the ratio of averaged water-leaving radiance Lw and downwelling irradiance, which may introduce a slight bias but is unlikely to affect our results here.) Two DoF remain in satellite climatological $R_{rs}(\lambda)$ for both SeaWiFS and MODIS-Aqua, indicating the possibility of generating two independent products from these data. The suite of products tested above, however, has one fewer DoF than the $R_{rs}(\lambda)$. This is likely due to derived products’ appreciable uncertainties and/or strong correlations with chlorophyll. POC, ξ , and Z_{eu} , for instance, have Spearman rank correlations (across all months and 1° grid cells) of >0.9 with Chl. C_{phyto} ’s rank correlation with Chl is still fairly high, at 0.61, and is low largely due to small fluctuations when both are small; a simple spline fit of $\log(C_{phyto})$ against $\log(\text{Chl})$ yields an r^2 of 0.7.

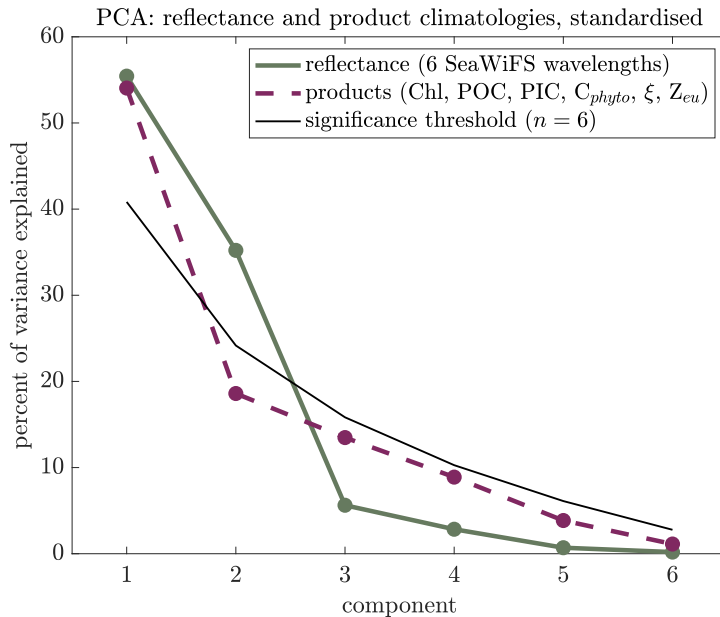


Figure 4. Scree plot of percent variance explained versus component for climatologies of SeaWiFS $R_{rs}(\lambda)$ and of six SeaWiFS- $R_{rs}(\lambda)$ -derived products. Black line indicates broken-stick significance threshold for six-dimensional data.

256 The exception is PIC, which has a rank correlation with Chl of 0.11. PIC, how-
 257 ever, is highly sensitive to small variations in $R_{rs}(\lambda)$ for typical $R_{rs}(\lambda)$ values. To sub-
 258 stantiate this, we performed a simple sensitivity analysis with the standard two-band PIC
 259 algorithm used by NASA for all but the most optically bright waters (see [https://oceancolor](https://oceancolor.gsfc.nasa.gov/atbd/pic/)
 260 [.gsfc.nasa.gov/atbd/pic/](https://oceancolor.gsfc.nasa.gov/atbd/pic/)). We calculated PIC for the climatological median $R_{rs}(\lambda)$
 261 at 443 nm and 555 nm and for 5% variations, converting to normalized water-leaving ra-
 262 diance by multiplying by the global mean extraterrestrial solar irradiance. We then per-
 263 turbed these $R_{rs}(\lambda)$ values with Gaussian noise at the 5% level, corresponding to the
 264 nominal uncertainty in $R_{rs}(\lambda)$. This noise at 443 nm results in 68% noise in PIC. By con-
 265 trast, POC only varies 5% with these 5% variations in $R_{rs}(\lambda)$ at either wavelength. This
 266 indicates that in the bulk of cases, satellite-derived PIC is highly uncertain, on the or-
 267 der of 70% (and note the PIC uncertainty will be magnified more when considering docu-
 268 mented uncertainties for $R_{rs}(\lambda)$ of 15-40% in some regions (Bisson et al., 2021)). In con-
 269 trast, for relatively bright waters, the same exercise resulted in PIC variations of <10%,
 270 indicating that this algorithm performs well in instances when PIC values are high. Nonethe-
 271 less, the high sensitivity to typical uncertainty in $R_{rs}(\lambda)$ for median waters explains why
 272 we find one DoF for the products even though PIC and Chl are not strongly correlated:
 273 derived PIC is noisy most of the time.

274 These results have two key implications. One is that there is additional informa-
 275 tion in climatological $R_{rs}(\lambda)$ that is not included in current derived products. This im-
 276 plies that existing products do not utilize the full set of $R_{rs}(\lambda)$ wavelengths. The other
 277 implication is that these products are not at all independent, and should not be treated
 278 as such when using them simultaneously. In other words, there are more products than
 279 there are DoF in satellite data. A numerical ecosystem model that reproduces the satellite-
 280 derived climatology of chlorophyll and of the particle size distribution's spectral slope
 281 should not be considered to be capturing two independent properties of the Earth sys-

282 tem. When using satellite products as inputs to other models, these products and their
 283 propagated uncertainties must be treated simultaneously rather than independently.

284 The results presented here are appropriate for global ocean analyses. The open ocean
 285 represents the largest area, and is composed primarily of Case 1 waters; that is, waters
 286 in which optical variability is dominated by chlorophyll (Morel & Prieur, 1977). In this
 287 context, it is in a sense unsurprising that the suite of $R_{rs}(\lambda)$ -derived products produced
 288 only one DoF. More optically complex waters, such as coastal regions and inland waters,
 289 have optical variability that is influenced by other constituents, such as colored dissolved
 290 organic material (CDOM), inorganic particles, and other pigments in addition to chloro-
 291 phyll (e.g. Brown et al., 2008; Nelson & Siegel, 2013)). Analyses focused on these wa-
 292 ters is likely to reveal a higher number of DoF from both $R_{rs}(\lambda)$ and derived products.
 293 Indeed, algorithms to derive concentrations of cyanobacteria and suspended particulate
 294 (Wang et al., 2016)) or distinguish between different phytoplankton species (Erickson
 295 et al., 2020) can be successful in such waters. However, we note that the in situ dataset
 296 used here (Figure 1) represents waters with $R_{rs}(\lambda)$ variability similar to that of the ocean
 297 as a whole, which can be seen by comparing the variation in $R_{rs}(\lambda)$ at each MODIS-Aqua
 298 wavelength from global satellite data with the same satellite data sub-sampled to the lo-
 299 cations with in situ measurements (or the closest non-cloudy location). Sub-sampled satel-
 300 lite measurements have similar, and slightly lower, $R_{rs}(\lambda)$ in bluer wavelengths, indicat-
 301 ing that the in situ dataset is oriented more towards optically complex coastal waters
 302 with substantial CDOM. This suggests that part of the explanation for the drop in DoF
 303 in satellite-derived climatologies comes from the fact that the in situ dataset sampled,
 304 as a whole, more optically complex waters.

305 We find that both $R_{rs}(\lambda)$ and variables derived from $R_{rs}(\lambda)$ are highly inter-correlated,
 306 reducing the number of DoF associated with each, with a greater reduction in DoF in
 307 the derived products. This becomes a problem when products are derived using empir-
 308 ical relationships with $R_{rs}(\lambda)$, and especially when the same wavelengths are used for
 309 the products that are assumed to be independent of each other; for example, over much
 310 of the ocean PIC, POC, and chlorophyll all are functions only of $R_{rs}(\lambda)$ at two wave-
 311 lengths, at (or near, depending on the sensor) 443 and 555 nm. Certain combinations
 312 of PIC, POC, and chlorophyll, which may occur in the surface ocean, are therefore im-
 313 possible to find using these algorithms. This is distinct from algorithms, typically called
 314 “quasi-analytical” or “semi-empirical”, that use known or assumed spectral shapes for
 315 absorption and scattering properties of optical constituents that can be related to the
 316 same derived products, such as PIC, POC, and chlorophyll (Werdell et al., 2013). These
 317 approaches may result in similar correlations and DoF between derived products, but
 318 do not inherently have the same problems as empirical approaches. We note that PACE
 319 will have, in addition to hyperspectral visible bands, UV bands from 350nm as well as
 320 spectral polarized bands. These measurements are expected to both improve the atmo-
 321 spheric correction (hence reduce the $R_{rs}(\lambda)$ uncertainties) as well as provide their own
 322 ocean signals, both of which may increase the DoF compared to those found here. In ad-
 323 dition, it has been shown that adding other environmental variables such as SST can add
 324 useful information to inversions of phytoplankton groups (e.g. Chase et al., 2022) and
 325 thus another approach to increase DoF for inversions by adding relevant and indepen-
 326 dent information (e.g. mixed-layer depth and nutrients from BGC-Argo assimilating mod-
 327 els).

328 4 Conclusion

329 The results presented here highlight the high degree of co-dependence between re-
 330 mote sensing reflectances at different wavelengths and of the products derived from these
 331 reflectances. For users of products based on existing reflectances, this primarily means
 332 factoring in the relationships between products when using more than one simultane-
 333 ously. For the algorithms that generate these products from existing reflectances, these

334 results indicate a potential to improve the suite of available products to be more accu-
335 rate and precise, and to account for the relationships between products and $R_{rs}(\lambda)$ wave-
336 bands. One way to do this, consistent with the findings above, would be to derive a sin-
337 gle product such as chlorophyll as a function of all reflectance wavebands, derive an anomaly
338 from chlorophyll-based expectations of a secondary product (e.g., phytoplankton com-
339 munity composition, size, POC, PIC, and so forth), then specify all other products ex-
340 plicitly as a function of these two, along the lines of Alvain et al. (2005). Ancillary and
341 independent information can also be added to algorithms, as is currently done with net
342 primary production models via temperature and mixed layer depth.

343 These findings are most relevant for algorithms that will generate products from
344 hyperspectral reflectances in the future. The small number of degrees of freedom in hy-
345 perspectral reflectances indicates that only a few quantities can be estimated indepen-
346 dently, and that different wavelengths' reflectances as measured from space will be strongly
347 correlated. Complex algorithms that utilize the full spectrum of reflectance will need to
348 factor in these correlations in order to generate reliable products. Crucially, if more than
349 a few products are generated from hyperspectral reflectances, as is likely the case, such
350 algorithms will also need to output the covariance information encoding the uncertainty
351 in each product and the relationships between them. This can be achieved by some, but
352 not all, machine learning techniques, on which this new generation of algorithms are likely
353 to be based. The fact that hyperspectral reflectances can be predicted within nominal
354 uncertainties by their multispectral equivalents suggests that hyperspectral resolution
355 can play a role in improving ocean color products, but that it will be challenging to pro-
356 vide a substantially finer-grained picture of surface ocean ecosystems and biogeochem-
357 ical cycles. Here by relying on principal component analysis we have focused on broad,
358 first-order variations, but where such resolution may be most useful and generate novel
359 insights is in investigating outliers and rare events, such as blooms or binning data over
360 coherent features like eddies, where e.g. monospecific signatures may be resolved with
361 spectral precision.

362 Open Research

363 Remote sensing data were downloaded from <https://oceancolor.gsfc.nasa.gov/>
364 and <http://sites.science.oregonstate.edu/ocean.productivity/index.php>. All
365 data and code are available at github.com/bbcael/eifoc for review purposes and will
366 be given a Zenodo DOI should this manuscript be accepted for publication.

367 Acknowledgments

368 It is a pleasure to thank the many scientists whose collective work has generated the data
369 on which this work relies. Cael acknowledges support from the National Environmen-
370 tal Research Council through Enhancing Climate Observations, Models and Data, and
371 the European Union's Horizon 2020 Research and Innovation Programme under grant
372 agreement No. 820989 (project COMFORT). The work reflects only the authors' view;
373 the European Commission and their executive agency are not responsible for any use that
374 may be made of the information the work contains. KB acknowledges support from NASA
375 grant 80NSSC18K0957. EB acknowledges support from NASA grant 80NSSC20M0203.
376 Cael lead and all other authors assisted with all aspects of this work. The authors have
377 no competing interests to declare. This is PMEL contribution number 5445.

378 References

379 Alvain, S., Moulin, C., Dandonneau, Y., & Breon, F.-M. (2005). Remote sensing of
380 phytoplankton groups in case 1 waters from global seawifs imagery. *Deep Sea*
381 *Research Part I: Oceanographic Research Papers*, 52(11), 1989–2004.

- 382 Behrenfeld, M. J., & Falkowski, P. G. (1997). Photosynthetic rates derived from
 383 satellite-based chlorophyll concentration. *Limnology and oceanography*, *42*(1),
 384 1–20.
- 385 Bisson, K., Boss, E., Werdell, P. J., Ibrahim, A., Frouin, R., & Behrenfeld, M.
 386 (2021). Seasonal bias in global ocean color observations. *Applied optics*,
 387 *60*(23), 6978–6988.
- 388 Bisson, K., Siegel, D. A., & DeVries, T. (2020). Diagnosing mechanisms of ocean
 389 carbon export in a satellite-based food web model. *Frontiers in Marine Sci-*
 390 *ence*, *7*, 505.
- 391 Brown, C. A., Huot, Y., Werdell, P. J., Gentili, B., & Claustre, H. (2008). The
 392 origin and global distribution of second order variability in satellite ocean
 393 color and its potential applications to algorithm development. *Remote*
 394 *Sensing of Environment*, *112*(12), 4186–4203. Retrieved from [https://](https://www.sciencedirect.com/science/article/pii/S0034425708002162)
 395 www.sciencedirect.com/science/article/pii/S0034425708002162 doi:
 396 <https://doi.org/10.1016/j.rse.2008.06.008>
- 397 Cael, B. (2021). Variability-based constraint on ocean primary production models.
 398 *Limnology and Oceanography Letters*, *6*(5), 262–269.
- 399 Cael, B., Bisson, K., & Follett, C. L. (2018). Can rates of ocean primary production
 400 and biological carbon export be related through their probability distributions?
 401 *Global biogeochemical cycles*, *32*(6), 954–970.
- 402 Cael, B., Bisson, K., & Follows, M. J. (2017). How have recent temperature changes
 403 affected the efficiency of ocean biological carbon export? *Limnology and*
 404 *Oceanography Letters*, *2*(4), 113–118.
- 405 Cael, B., Chase, A., & Boss, E. (2020). Information content of absorption spectra
 406 and implications for ocean color inversion. *Applied Optics*, *59*(13), 3971–3984.
- 407 Cael, B., Dutkiewicz, S., & Henson, S. (2021). Abrupt shifts in 21st-century plank-
 408 ton communities. *Science advances*, *7*(44), eabf8593.
- 409 Campbell, J. W. (1995). The lognormal distribution as a model for bio-optical vari-
 410 ability in the sea. *Journal of Geophysical Research: Oceans*, *100*(C7), 13237–
 411 13254.
- 412 Chase, A. P., Boss, E., Cetinić, I., & Slade, W. (2017). Estimation of phytoplankton
 413 accessory pigments from hyperspectral reflectance spectra: toward a global
 414 algorithm. *Journal of Geophysical Research: Oceans*, *122*(12), 9725–9743.
- 415 Chase, A. P., Boss, E. S., Haëntjens, N., Culhane, E., Roesler, C., & Karp-Boss,
 416 L. (2022). Plankton imagery data inform satellite-based estimates of diatom
 417 carbon. *Geophysical Research Letters*, *49*(13), e2022GL098076. Retrieved
 418 from [https://agupubs.onlinelibrary.wiley.com/doi/abs/10.1029/](https://agupubs.onlinelibrary.wiley.com/doi/abs/10.1029/2022GL098076)
 419 [2022GL098076](https://agupubs.onlinelibrary.wiley.com/doi/abs/10.1029/2022GL098076) (e2022GL098076 2022GL098076) doi: [https://doi.org/10.1029/](https://doi.org/10.1029/2022GL098076)
 420 [2022GL098076](https://doi.org/10.1029/2022GL098076)
- 421 DeVries, T., & Weber, T. (2017). The export and fate of organic matter in the
 422 ocean: New constraints from combining satellite and oceanographic tracer
 423 observations. *Global Biogeochemical Cycles*, *31*(3), 535–555.
- 424 Dutkiewicz, S., Cermenó, P., Jahn, O., Follows, M. J., Hickman, A. E., Taniguchi,
 425 D. A., & Ward, B. A. (2020). Dimensions of marine phytoplankton diversity.
 426 *Biogeosciences*, *17*(3), 609–634.
- 427 Erickson, Z. K., Werdell, P. J., & Cetinić, I. (2020). Bayesian retrieval of optically
 428 relevant properties from hyperspectral water-leaving reflectances. *Applied Op-*
 429 *tics*, *59*(23), 6902–6917. doi: 10.1364/AO.398043
- 430 Evers-King, H., Martínez-Vicente, V., Brewin, R. J., Dall’Olmo, G., Hickman, A. E.,
 431 Jackson, T., ... others (2017). Validation and intercomparison of ocean color
 432 algorithms for estimating particulate organic carbon in the oceans. *Frontiers*
 433 *in Marine Science*, 251.
- 434 Gordon, H. R., & Wang, M. (1994). Retrieval of water-leaving radiance and aerosol
 435 optical thickness over the oceans with seawifs: a preliminary algorithm. *Ap-*
 436 *plied optics*, *33*(3), 443–452.

- 437 Graff, J. R., Westberry, T. K., Milligan, A. J., Brown, M. B., Dall’Olmo, G., van
 438 Dongen-Vogels, V., . . . Behrenfeld, M. J. (2015). Analytical phytoplankton
 439 carbon measurements spanning diverse ecosystems. *Deep Sea Research Part I:
 440 Oceanographic Research Papers*, *102*, 16–25.
- 441 Hovis, W. A., Clark, D., Anderson, F., Austin, R., Wilson, W., Baker, E., . . . others
 442 (1980). Nimbus-7 coastal zone color scanner: system description and initial
 443 imagery. *Science*, *210*(4465), 60–63.
- 444 Hu, C., Lee, Z., & Franz, B. (2012). Chlorophyll algorithms for oligotrophic oceans:
 445 A novel approach based on three-band reflectance difference. *Journal of Geo-
 446 physical Research: Oceans*, *117*(C1).
- 447 Huot, Y., & Antoine, D. (2016). Remote sensing reflectance anomalies in the ocean.
 448 *Remote Sensing of Environment*, *184*, 101–111. doi: 10.1016/j.rse.2016.06.002
- 449 Jackson, D. A. (1993). Stopping rules in principal components analysis: a compari-
 450 son of heuristical and statistical approaches. *Ecology*, *74*(8), 2204–2214.
- 451 Kostadinov, T., Siegel, D., & Maritorena, S. (2009). Retrieval of the particle size
 452 distribution from satellite ocean color observations. *Journal of Geophysical Re-
 453 search: Oceans*, *114*(C9).
- 454 Kramer, S. J., Siegel, D. A., Maritorena, S., & Catlett, D. (2022). Modeling surface
 455 ocean phytoplankton pigments from hyperspectral remote sensing reflectance
 456 on global scales. *Remote Sensing of Environment*, *270*, 112879.
- 457 Lee, Z., Weidemann, A., Kindle, J., Arnone, R., Carder, K. L., & Davis, C. (2007).
 458 Euphotic zone depth: Its derivation and implication to ocean-color remote
 459 sensing. *Journal of Geophysical Research: Oceans*, *112*(C3).
- 460 Mitchell, C., Hu, C., Bowler, B., Drapeau, D., & Balch, W. (2017). Estimating par-
 461 ticulate inorganic carbon concentrations of the global ocean from ocean color
 462 measurements using a reflectance difference approach. *Journal of Geophysical
 463 Research: Oceans*, *122*(11), 8707–8720.
- 464 Morel, A., & Prieur, L. (1977). Analysis of variations in ocean color 1. *Limnology
 465 and oceanography*, *22*(4), 709–722.
- 466 Nelson, N. B., & Siegel, D. A. (2013). The global distribution and dynamics of chro-
 467 mophoric dissolved organic matter. *Annual review of marine science*, *5*, 447–
 468 476.
- 469 Nowicki, M., DeVries, T., & Siegel, D. A. (2022). Quantifying the carbon export and
 470 sequestration pathways of the ocean’s biological carbon pump. *Global Biogeo-
 471 chemical Cycles*, *36*(3), e2021GB007083.
- 472 O’Reilly, J. E., Maritorena, S., Mitchell, B. G., Siegel, D. A., Carder, K. L., Garver,
 473 S. A., . . . McClain, C. (1998). Ocean color chlorophyll algorithms for seawifs.
 474 *Journal of Geophysical Research: Oceans*, *103*(C11), 24937–24953.
- 475 Scholz, M., Fraunholz, M., & Selbig, J. (2008). Nonlinear principal component anal-
 476 ysis: neural network models and applications. In *Principal manifolds for data
 477 visualization and dimension reduction* (pp. 44–67). Springer.
- 478 Scott, J. P., & Werdell, P. J. (2019). Comparing level-2 and level-3 satellite ocean
 479 color retrieval validation methodologies. *Optics Express*, *27*(21), 30140–30157.
- 480 Siegel, D., Buesseler, K., Doney, S. C., Sailley, S., Behrenfeld, M. J., & Boyd, P.
 481 (2014). Global assessment of ocean carbon export by combining satellite obser-
 482 vations and food-web models. *Global Biogeochemical Cycles*, *28*(3), 181–196.
- 483 Silsbe, G. M., Behrenfeld, M. J., Halsey, K. H., Milligan, A. J., & Westberry, T. K.
 484 (2016). The cafe model: A net production model for global ocean phytoplankton.
 485 *Global Biogeochemical Cycles*, *30*(12), 1756–1777.
- 486 Wang, G., Lee, Z., Mishra, D. R., & Ma, R. (2016). Retrieving absorption coef-
 487 ficients of multiple phytoplankton pigments from hyperspectral remote sens-
 488 ing reflectance measured over cyanobacteria bloom waters. *Limnology and
 489 Oceanography: Methods*, *14*(7), 432–447. doi: 10.1002/lom3.10102
- 490 Weinberger, K. Q., Sha, F., & Saul, L. K. (2004). Learning a kernel matrix for non-
 491 linear dimensionality reduction. In *Proceedings of the twenty-first international*

- 492 *conference on machine learning* (p. 106).
- 493 Werdell, P. J., Behrenfeld, M. J., Bontempi, P. S., Boss, E., Cairns, B., Davis,
494 G. T., ... others (2019). The plankton, aerosol, cloud, ocean ecosystem
495 mission: status, science, advances. *Bulletin of the American Meteorological*
496 *Society*, 100(9), 1775–1794.
- 497 Werdell, P. J., Franz, B. A., Bailey, S. W., Feldman, G. C., Boss, E., Brando, V. E.,
498 ... others (2013). Generalized ocean color inversion model for retrieving
499 marine inherent optical properties. *Applied Optics*, 52(10), 2019–2037.
- 500 Westberry, T., Behrenfeld, M., Siegel, D., & Boss, E. (2008). Carbon-based primary
501 productivity modeling with vertically resolved photoacclimation. *Global Bio-*
502 *geochemical Cycles*, 22(2).
- 503 Wold, S., Esbensen, K., & Geladi, P. (1987). Principal component analysis. *Chemo-*
504 *metrics and intelligent laboratory systems*, 2(1-3), 37–52.